Stochastic nature of incipient plasticity in a body-centered cubic medium-entropy alloy

A-Hyun Jeon[1,⊥], Yakai Zhao[2,⊥], Zhe Gao[1], Jin-Yoo Suh[3], Ho Jin Ryu[4], Hyoung Seop Kim[5,6,7], Upadrasta Ramamurty[2,8], Jae-il Jang[1,*]

[1]Division of Materials Science and Engineering, Hanyang University, Seoul 04763, Republic of Korea
[2]Institute of Materials Research and Engineering (IMRE), Agency for Science, Technology and Research (A*STAR), Singapore 138634, Republic of Singapore
[3]Center for Energy Materials Research, Korea Institute of Science and Technology (KIST), Seoul 02792, Republic of Korea
[4]Department of Nuclear and Quantum Engineering, Korea Advanced Institute of Science and Technology (KAIST), Daejeon 34141, Republic of Korea
[5]Graduate Institute of Ferrous & Eco Materials Technology, Pohang University of Science and Technology (POSTECH), Pohang 37673, Republic of Korea
[6]Advanced Institute for Materials Research (WPI-AIMR), Tohoku University, Sendai, 980-8577, Japan
[7]Institute for Convergence Research and Education in Advanced Technology, Yonsei University, Seoul 03722, Republic of Korea
[8]School of Mechanical and Aerospace Engineering, Nanyang Technological University, Singapore 639798, Republic of Singapore

⊥ These authors contributed equally to this work.

*Corresponding author: jijang@hanyang.ac.kr (J.-i. Jang)

ABSTRACT

The stochastic nature of the small-scale incipient plasticity (i.e., "pop-in" behavior manifested as a sudden displacement excursion in the load-displacement curves) in a single grain of the body-centered cubic NbTiZr medium-entropy alloy is explored through a series of nanoindentation tests with three spherical tips having different radii (1.8, 3.4, and 8.2 μm). The maximum shear stress underneath the indenter shows distinct distributions depending on the tip radius, wherein both a narrow high-stress regime and a broad low-stress regime are observed. By recourse to deconvolution of the data and detailed statistical analysis, the two regimes were found to be dominated by homogeneous and heterogeneous yielding mechanisms, respectively. Upon hydrogen charging, the tip radius dependence is sustained, but the fraction of heterogeneous yielding is enhanced, which is due to the hydrogen's effect in assisting defect formation. The suggested scenarios for how the mechanisms are affected by the stressed volume (or tip radius) and hydrogen-induced structural changes were confirmed by direct observations of the deformation behavior underneath the indenter with cross-sectional transmission electron microscopy made on post-pop-in samples.

Keywords: Medium-entropy alloy; incipient plasticity; hydrogen; nanoindentation.

1. Introduction

Research conducted over the past four decades has established the nanoindentation testing technique to be the most robust tool for characterizing the mechanical behavior of materials at the small scales in both quantitative and qualitative manner [1–3]. While hardness and effective modulus are the most widely measured mechanical properties using it, various other small-scale mechanical responses have been also actively studied. One of them is the incipient plasticity. Page *et al.* [4] were the first one to correlate the "pop-in" (or discrete displacement burst) observed during the loading segment of the load-displacement curve obtained (using a spherical tipped indenter) on well-annealed crystalline ceramics with the dislocation loop nucleation. Since then, the small-scale yielding or elastic-to-elastoplastic transition has been investigated extensively not only in crystalline materials but also in metallic glasses and molecular crystals [3,5,6], by analyzing the pop-in behavior.

Although the intrinsic nature of the pop-in and related phenomena has not yet been completely understood (and hence studies continue to be performed), the following two are the common features of it. First, the first pop-in is stochastic in nature, i.e., a series of nanoindentations performed under identical experimental conditions result in a pop-in load data that is often widespread. This means a thorough statistical analysis of the pop-in data is imperative [7–10]. Second, varying the experimental conditions (such as the indentation rate, temperature, and indenter radius) often affects the measured dispersions in the pop-in load [11–13]. Among the three experimental variables, the influence of strain rate and temperature on the yield strength is reasonably well understood through the conventional macro- and micro-scale uniaxial tests [14], which makes the interpretation straightforward. However, the third experimental variable, indenter radius (R_i), can be accessed only in the context of the nanoindentation tests (performed with the spherical (or rounded) tips). It enables probing the size dependence of incipient plasticity, as R_i directly scales with the size of the highly stressed volume underneath the indenter. Although one can gain a detailed understanding of the predominant mechanisms of incipient plasticity by varying R_i, relatively fewer studies examined this aspect. To the best of our knowledge, only six metallic materials were studied, including face-centered cubic (fcc) single crystals (SCs) of Ni [13] and Fe-15Cr-15Ni [15]; body-centered cubic (bcc) SCs of Mo [7,9,10,16,17], Mo-3Nb [18], and W [17,19]; a Zr-Cu-Ni-Al-Ti bulk metallic glass (commercially called Vit105) [20–22].

Keeping the above in view, we conducted a series of nanoindentation tests on a NbTiZr medium-entropy alloy (MEA) with three spherical indenters having different R_i in this study with the following three objectives. First, to explore the stochastic nature of incipient plasticity in the single-phase equiatomic MEA with the bcc crystal structure. Selecting NbTiZr provides an additional important merit: the average grain size of the examined sample is sufficiently large (~2 mm) such that all the indentations could be made in a single grain, i.e., single crystalline response could be obtained. Thus, the results are free from the influence of crystallographic orientation. Second, with the aid of the estimated activation volume for the onset of plastic deformation and cross-sectional transmission electron microscopy (TEM) analysis, elucidate the effect of deformed volume (through the variation of R_i) on the mechanisms of incipient plasticity in this SC MEA. The final objective is to examine the effect of hydrogen on the stochastic nature and small-scale yielding mechanisms. It is well known that hydrogenation of an alloy could affect the microstructural features in it through the interaction between hydrogen and defects, such as dislocations [23], deformation twins [24], and vacancies [25], which, in turn, could lead to mechanical degradation ("hydrogen embrittlement"). The presence of hydrogen in alloy could also affect the incipient plasticity significantly by altering state/mobility of various defects. Therefore, a detailed study is likely to provide critical insights on the role of hydrogen on the yielding mechanism of an alloy [26].

2. Experiments

The equiatomic NbTiZr MEA examined in this study was arc melted, then cold-rolled to a thickness reduction of 40% and subsequently annealed at 1400 °C. The microstructure of the sample was characterized using electron backscatter diffraction (EBSD; Hikari, EDAX-TSL, USA) and X-ray diffraction (XRD; Bruker D8, Germany). For the EBSD and nanoindentation measurements, the samples were mechanically polished first with sandpapers (grit number up to 2000) and then electropolished with 20 V for 30 s at −25 °C in a mixture of 90% methanol and 10% perchloric acid. Hydrogen charging was conducted on the mechanically polished samples electrochemically at room temperature (RT, ~25 °C) with a current density of 100 mA/cm^2 for 24 h in a 1:2 (vol.) H_3PO_4:glycerine solution in a potentiostat/galvanostat equipment.

Nanoindentation tests on uncharged and hydrogen-charged specimens were performed using the Nanoindenter-XP instrument (KLA, USA) with three spherical indenters of tip radii, R_i = 1.8, 3.4, and 8.2 μm. Various loading rates dP/dt = 0.1, 0.25, 0.5, and 1 mN/s and peak loads P_{max} = 10, 20, and 80 mN were utilized and the tests were always performed under load control. The horizontal and vertical spacing between neighboring indents was maintained to be at least 20 μm. More than 100 indentations were performed for each experimental condition to obtain statistically significant data. All the nanoindentations were performed well inside pre-identified grain(s) and away from adjacent grain boundaries, so that all the influence of grain boundaries on the differences observed in the pop-in behavior is ruled out. In selected cases, dislocation distribution underneath the indenter impression was investigated using TEM (Titan 80-300, FEI, USA), for which the samples were prepared using the focused ion beam (FIB; NX5000, Hitachi, Japan) milling with Ga ions first and then Ar ions. Ar ions were used to reduce the ion damage on the sample surface that would affect the subsequent TEM observations of dislocations [27]. For comparison with the nanoindentation data, Young's modulus (E) and Poisson's ratio (v) of the samples were also measured with the aid of ultrasonic pulse-echo testing equipment (Nawoo, Korea) following the ASTM E-494 standard.

3. Results

3.1. Microstructure

The XRD scan obtained on the NbTiZr MEA is shown in Fig. 1a, demonstrating a single bcc phase, which agrees well with the previous reports [20,21]. Fig. 1b shows the representative inverse pole figure (IPF) images obtained using EBSD. It is evident that the examined NbTiZr MEA consists of equiaxed grains with very large average grain size, d, of ~2 mm, which makes it possible to easily obtain sufficient nanoindentation data from a single grain. In the present paper, all the subsequent nanoindentation experiments were conducted on "Grain 1" that is (9 1 3) oriented, and thus all the data are for the grain unless otherwise specified. Some additional indentation tests were also performed on "Grain 2" with (11 10 13) orientation, in order to confirm the stochastic nature obtained from Grain 1 is representative for the examined MEA. These two grains were selected because of their relatively large grain size (approximately 2 mm). In all cases, it was ensured that the nanoindentations are sufficiently far away from the grain boundaries, such that the grain boundaries have no influence on the measured response.

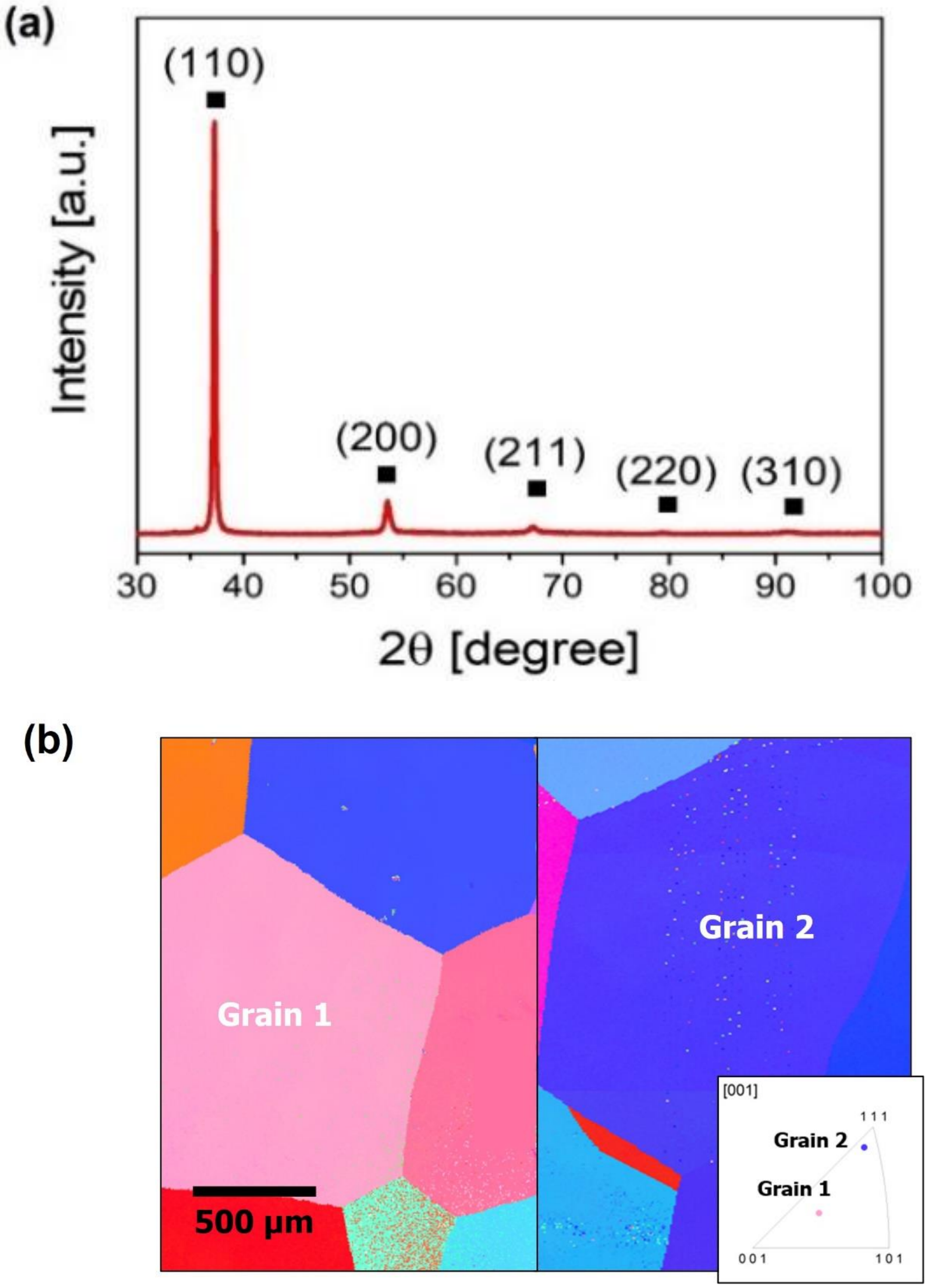

Fig. 1 Microstructural characterization of the NbTiZr MEA examined in this study: (a) XRD pattern and (b) the grains probed identified on the EBSD inverse pole figure (IPF) maps.

3.2. Nanoindentation

Representative examples of the load-displacement (*P*–*h*) responses, measured with three indenter tips having different R_i, are displayed in Fig. 2. Discrete displacement bursts or "pop-ins" are evident in all the cases. While the load at which the first pop-in occurs (P_I) increases with R_i, it also stochastic in nature. The P-h responses before and after the pop-ins are fully elastic and, hence, are unique for a given R_i. To ascertain this, the load P vs. depth of penetration h relation obtained from the Hertzian elastic contact theory [22], $P = \frac{4}{3}E_r R_i^{\frac{1}{2}} h^{\frac{3}{2}}$ (where E_r is the reduced modulus, $\frac{1}{E_r} = \frac{(1-v_s{}^2)}{E_s} + \frac{(1-v_i{}^2)}{E_i}$, in which the subscripts i and s are indenter and sample, respectively), was fitted to the data before the first pop-in occurs. The E_r values obtained are listed in Table 1. They are in good agreement with those measured using ultrasonic pulse-echo tests. Note also that the values E_r obtained from indentations are independent of R_i, as expected.

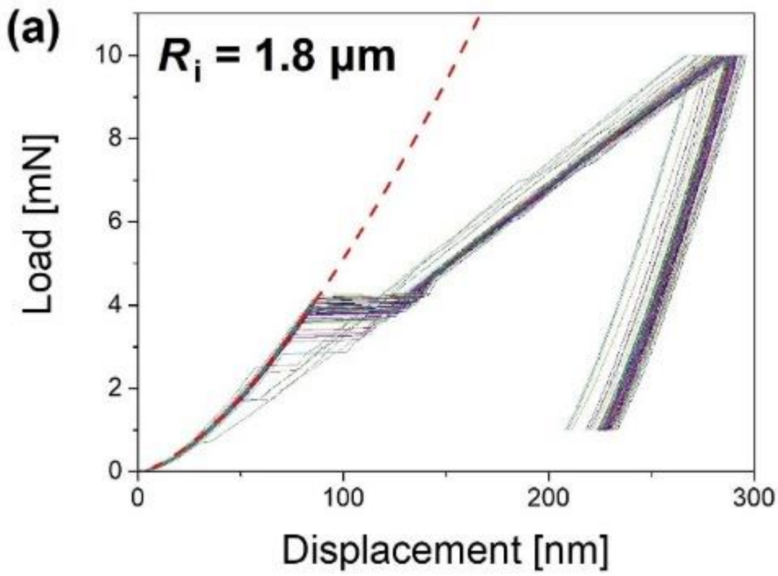

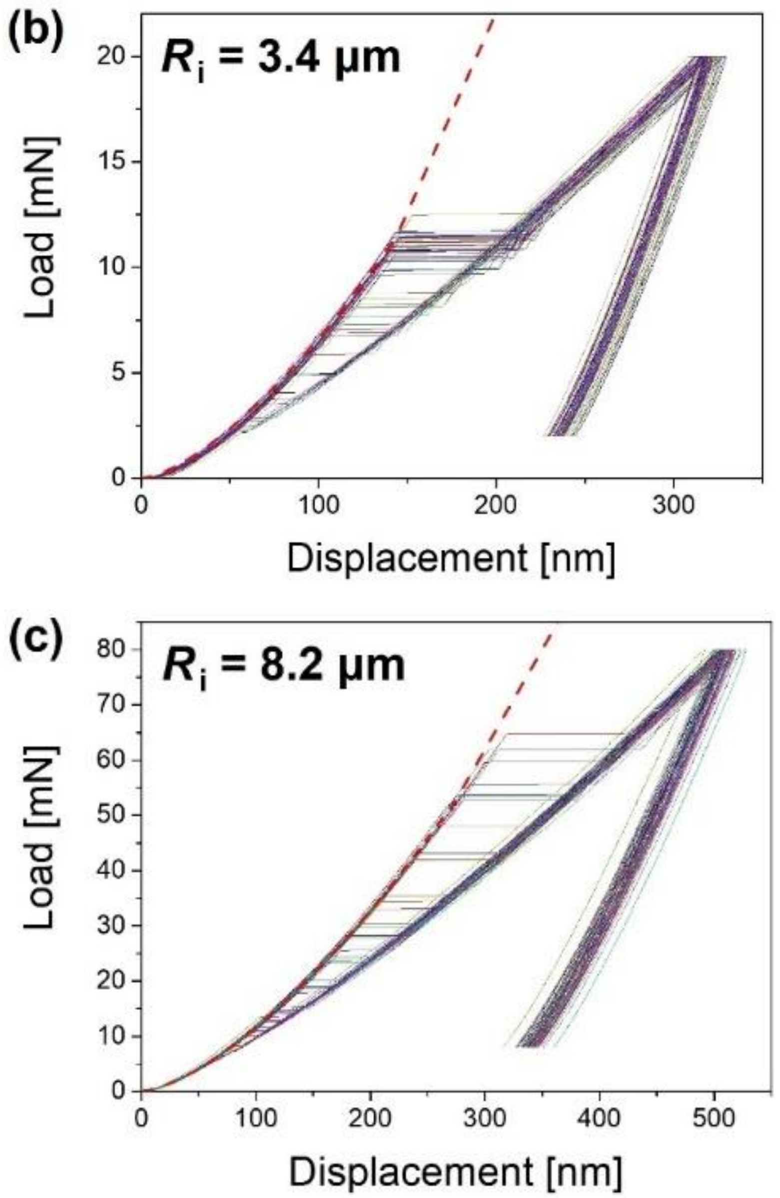

Fig. 2 Typical load-displacement (*P*-*h*) curves for the tests with (a) R_i = 1.8, (b) 3.4, and (c) 8.2 μm.

Table 1 Summary of the *v*, *E*, and E_r results obtained from ultrasonic pulse-echo tests and spherical indentation tests.

	R_i [μm]	*v*	*E* [GPa]	E_r [GPa]
Ultrasonic data	–	0.38	84.5 ± 6.4	90.6 ± 5.3
Indentation data	1.8	–	–	90.4 ± 1.6
	3.4	–	–	83.8 ± 1.6
	8.2	–	–	93.5 ± 6.6

The cumulative probability distributions of P_I for all the indentation experiments performed with three different tips under four different loading rates, dP/dt (0.1, 0.25, 0.5, and 1 mN/s) are plotted in Fig. 3. Two features are evident. First, the rate dependency of the statistical distribution is insignificant and almost negligible. This is in contrast to the prior report on Pt [11,12], but similar to that on Mo and Ni [28], implying the rate dependency of pop-in behavior may be affected by elemental nature, microstructures, and slip systems. Second, and more importantly, the shape of the distribution varies with R_i, which will be analyzed in detail in subsequent sections.

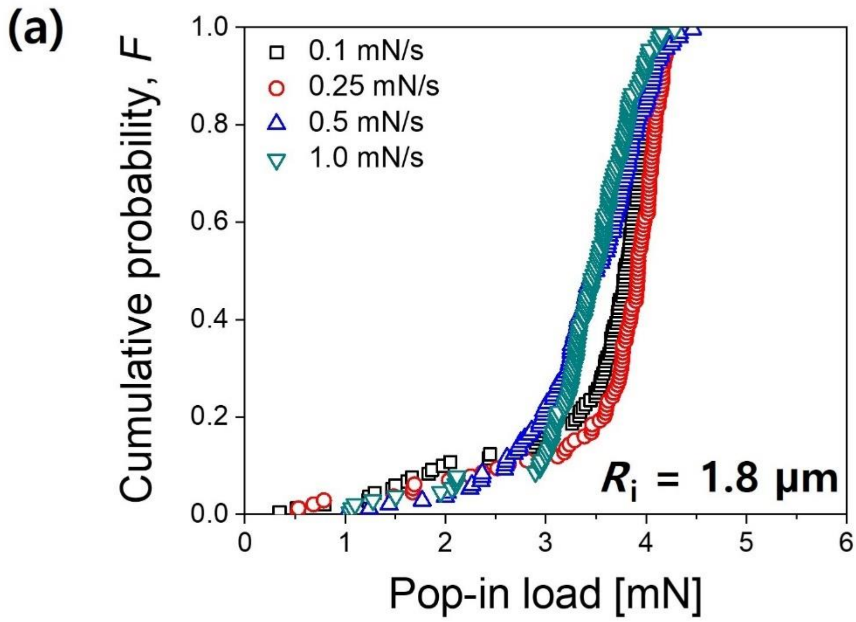

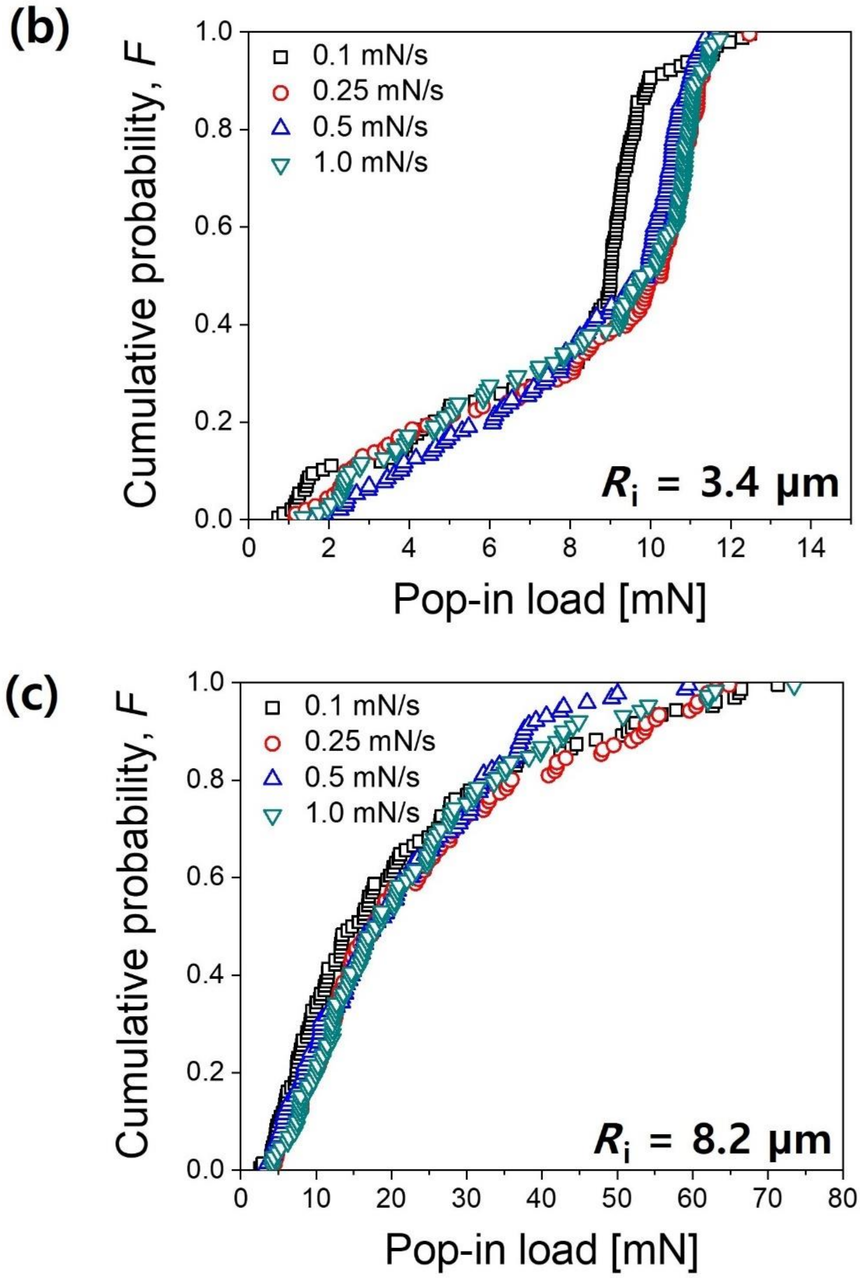

Fig. 3 Cumulative probability distributions of the first pop-in loads for the tests performed with three indenter tips of R_i = (a) 1.8, (b) 3.4, and (c) 8.2 μm (with four different loading rates of 0.1, 0.25, 0.5, and 1 mN/s).

The maximum shear stress beneath a spherical indenter at the first pop-in, τ_y, is estimated using the relation [22]:

$$\tau_y = 0.31\left(\frac{6P_I E_r^{2}}{\pi^3 R_i^{2}}\right)^{\frac{1}{3}}. \quad (1)$$

Variations in τ_y are displayed in Fig. 4 as cumulative probability distribution plots. The following two key observations can be made from it. (1) The τ_y range shifts to higher stresses with decreasing R_i. (2) The shape of the distribution varies significantly with R_i. For the smallest R_i used in this study (1.8 μm), the cumulative probability F vs. τ_y data appears bilinear, with most of it confined to a narrow range (~3.5–3.9 GPa). The data obtained with the largest R_i (8.2 μm) is uniformly distributed over a wider range (~1.3–3.5 GPa). The data for R_i = 3.4 μm is also bilinear, but with equal shares of narrow and wider distributed τ_y.

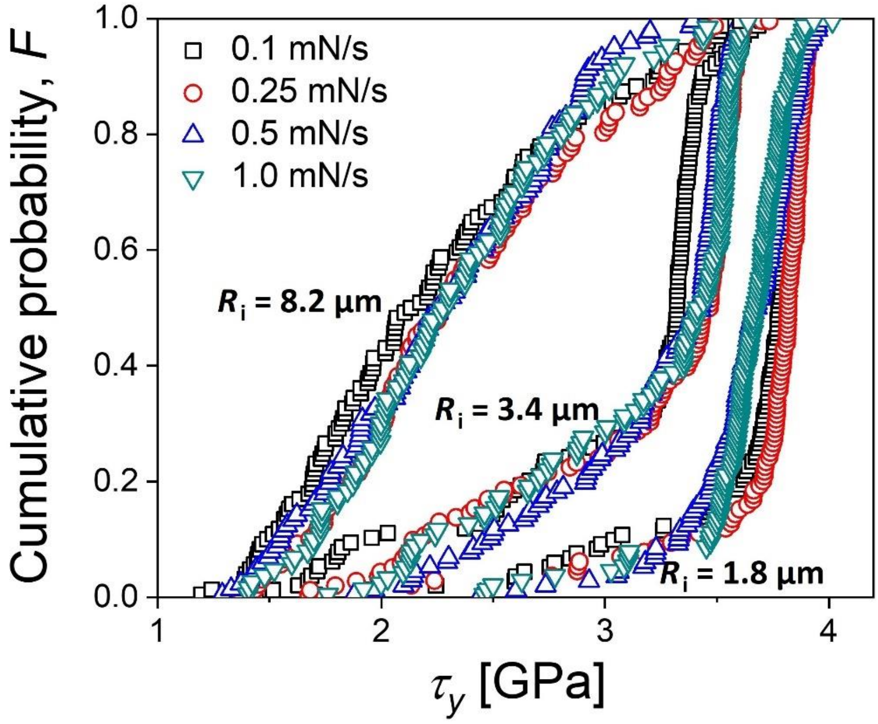

Fig. 4 Cumulative probability distributions plotted as a function of the maximum shear stresses at the first pop-in (τ_y).

4. R_i-dependent stochastic nature of pop-in

A decrease in τ_y with increasing R_i has been reported for single-crystal metals [9,10,12], which was often referred to as a different type of "indentation size effect" [13]. It is closely related to the microscopic yielding mechanisms mediated by the dislocations. Different governing mechanisms cause P_I and, consequently, τ_y as well as their distribution shapes to differ. Fig. 5 schematically illustrates the deformation mechanisms that are likely to be sampled at different R_i. (It was drawn on the basis of already available understanding on the role of R_i on the first pop-in behavior [2,10].) For a sufficiently small R_i, the volume of the highly stressed region underneath the indenter is very small (often in nm^3 range) [7,13]. The probability for the stressed region to contain either pre-existing dislocation(s) or other types of crystalline defects (vacancies, grain boundaries, etc.) is low. Therefore, pop-in in this defect-free case will only get triggered when dislocations get nucleated homogeneously. This is referred to as "homogeneous yielding" hereafter. Such a mechanism is fairly difficult to get activated in crystalline materials since it can only happen in a defect-free perfect lattice (at least locally). Importantly, it requires a very high applied stress that typically approaches the athermal theoretical shear strength of the material (~$G/30$–$G/5$, where G is shear modulus [13]). In general, the τ_y distribution for homogeneous yielding is narrow, as illustrated by the red curve in Fig. 5, since the scatter may be purely due to the thermal fluctuation, i.e., in the high applied stress regime slightly below the athermal theoretical strength, the energy barrier can be overcome by thermal fluctuations [7,8]. While a broader range of $G/30$–$G/5$ for τ_y under homogeneous yielding conditions is estimated [13,28], many prior studies suggest that it to be narrower, ranging between $G/2\pi$ and $G/10$ [29]. In the present context, some of the τ_y values for non-homogeneous yielding (at the higher end) can be higher than the lower bound ($G/30$), as shown later, which is reflected in the schematic illustration provided in Fig. 5.

For sufficiently large R_i, the size of the highly stressed region would also be large. This results in a high likelihood of pre-existing dislocations and/or other defects (such as vacancies, vacancy clusters, immobile dislocations, and impurities) being present in the volume being probed. Under such circumstances, the pop-ins are more likely to result from the following two types of dislocation activities: (1) heterogeneous dislocation nucleation aided by the pre-existing defects (followed by dislocation avalanches) and (2) activation of the glide of pre-existing mobile dislocations [2,4,10,13]. These two mechanisms are collectively referred to as "heterogeneous yielding" hereafter. The stress required for the elastic-to-elastoplastic transition (*viz*. pop-in stress) in this scenario would be much lower than that required for homogeneous yielding and is predominated by spatial statistics of the pre-existing defects rather than thermal fluctuation-induced ones [2,7,8]. This, consequently, results in a widespread of τ_y, as illustrated by the blue curve in Fig. 5.

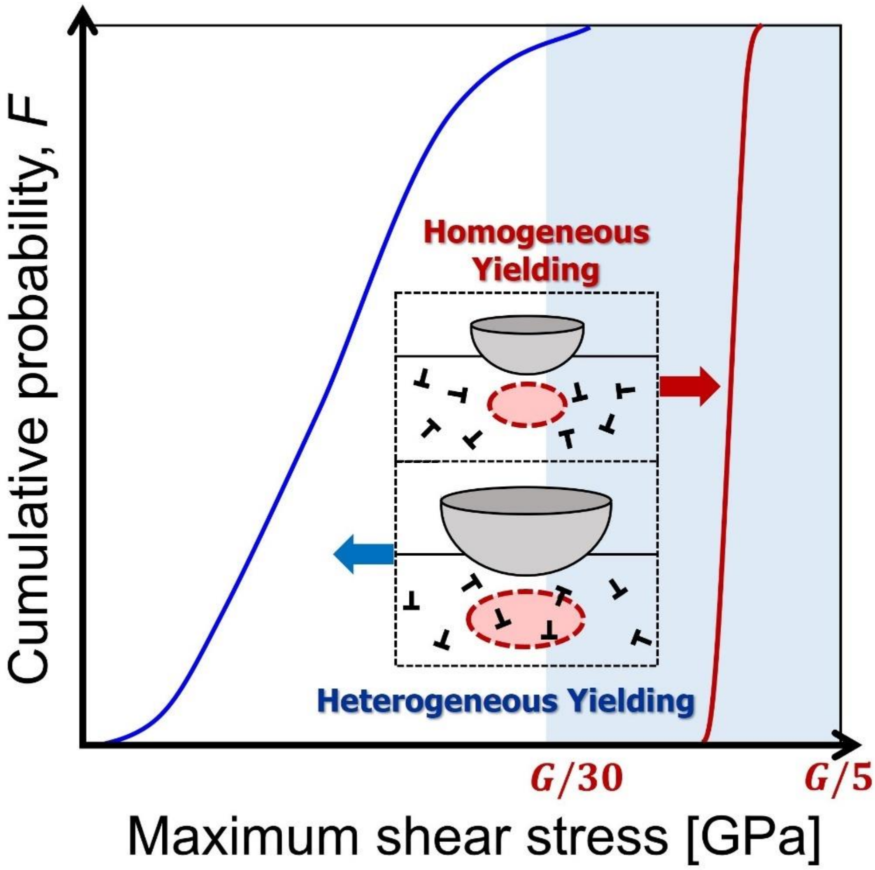

Fig. 5 Schematic illustration of effect of probed volume (via the variation of the tip radius) on the maximum shear stress underneath the indenter at the first pop-in.

Fig. 6 shows the cumulative probability distributions of τ_y obtained at 0.25 mN/s at various R_i. For R_i = 1.8 μm, most of the data are narrowly distributed in the high τ_y region. Only a few data points are located in the low τ_y regime and occur with relatively higher dispersion. This suggests that when a small-tipped indenter is used, the incipient plasticity mainly occurs due to homogeneous yielding, with a rather marginal probability of heterogeneous yielding. The average τ_y value in the homogeneous yielding regime is ~3.84±0.05 GPa, which corresponds to ~G/8 (G = ~30.6 GPa based on the results from ultrasonic pulse-echo tests in Table 1) and hence, falls within the range of theoretical shear strength [13]. This observation further confirms that the narrowly distributed and high τ_y values correspond to homogeneous yielding. The nearly-deterministic nature of τ_y in this regime is possibly because plastic event in this case is always triggered at (or very near) the location of the maximum shear stress underneath the spherical indenter tip (about 0.48a away from the point of contact [9]).

For the τ_y data obtained with R_i = 8.2 μm, the cumulative probability distribution has a gentle slope overall, indicating that yielding mainly occurs due to heterogeneous rather than homogeneous yielding. For the intermediate case with R_i = 3.4 μm, the τ_y data are almost evenly distributed in both regions, indicating that both homogeneous and heterogeneous yielding mechanisms substantially contribute to the yielding behavior, i.e., if the highly stressed region underneath the indenter contains any pre-existing defects, they would get activated at relatively low indentation loads, resulting in heterogeneous yielding. As the indentation load increases, the size of the highly stressed region increases. If the enlarged region does not encounter any pre-existing defects until the stress approaches the theoretical strength, yielding can occur by homogenous dislocation nucleation. Similar results to those in Fig. 6 were also observed for indentations made on Grain 2, as shown in Fig. S1, indicating the trend in Fig. 6 is representative of MEA examined in the present study.

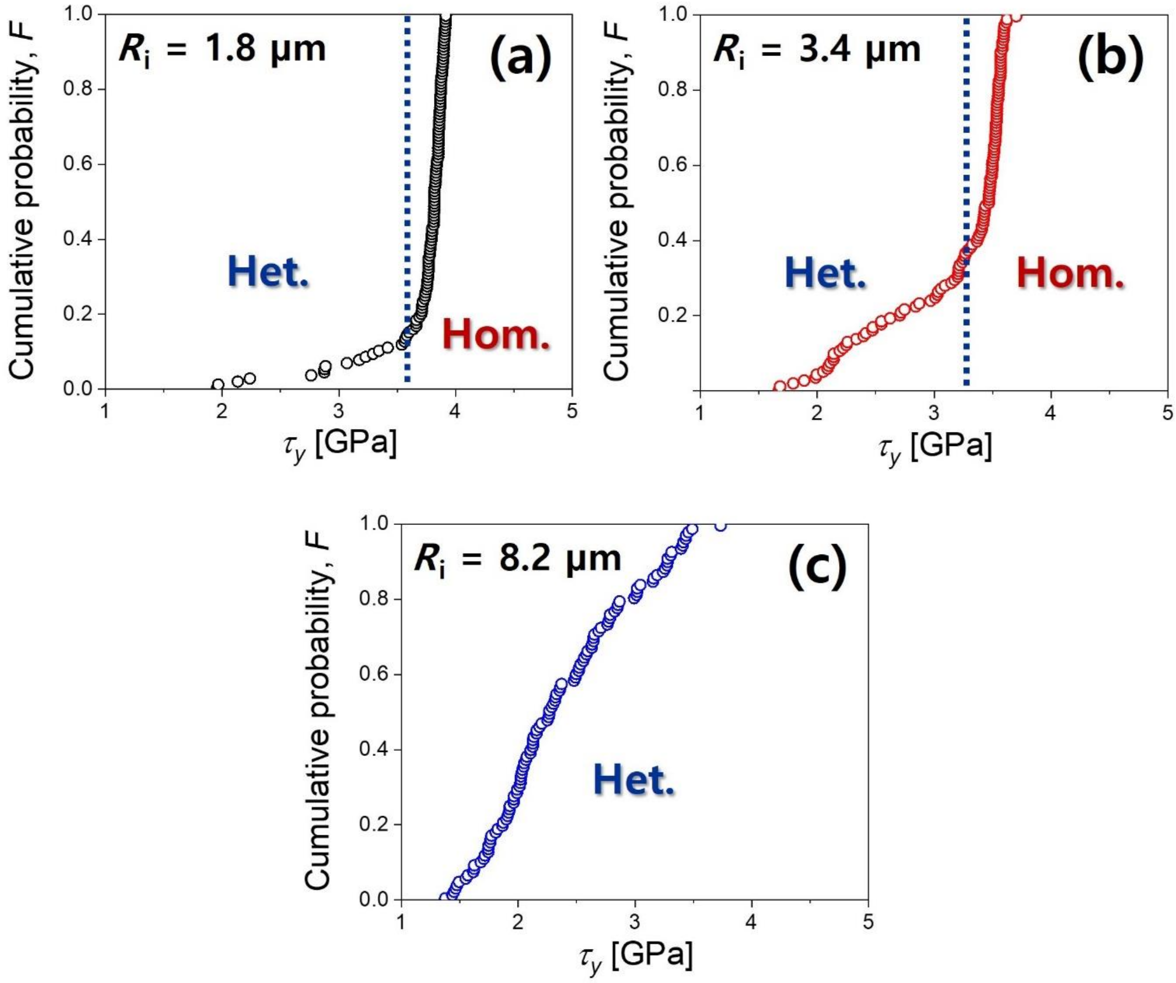

Fig. 6 Cumulative probability distribution curves at 0.25 mN/s of R_i = (a) 1.8, (b) 3.4, and (c) 8.2 μm. (Het.: heterogeneous yielding, Hom.: homogeneous yielding)

The F vs. τ_y data is often utilized to estimate the activation volume, V^*, of the microstructural source causing the incipient plasticity, using the relation [9,30–33]:

$$F = 1 - \exp\left[-\exp\left(\frac{V^*}{kT}\tau_y + \beta\right)\right] \tag{2}$$

where k is the Boltzmann constant, T is the absolute temperature, and β is a weak function of P_I [12,32]. Typically, the experimental data tends to be linear when plotted as ln[−ln(1−F)] versus τ_y, the slope of which is utilized to obtain V^* [12,31–34]. While reasonably good linear fits could be obtained for the data measured with R_i = 1.8 and 8.2 μm (since homogeneous and heterogeneous yielding, respectively, dominate them), the results with R_i = 3.4 μm do not follow a single linear trend when plotted on a ln[−ln(1−F)] scale. This observation further supports our hypothesis that the yielding behavior in this case is not governed by a single type of deformation mechanism. Therefore, separate fittings were carried out for homogeneous and heterogeneous yielding regimes for the data at R_i = 3.4 μm, as shown in the inset of Fig. 7. V^* were obtained from the slopes according to Eq. (2) and their normalized values (with the atomic volume, $\Omega = 0.5a^3$ for bcc structure, where a = ~0.34 nm for NbTiZr [35]) are displayed in Fig. 7 alongside the corresponding curves shown in the inset. For the initiation of plasticity due to homogeneous yielding with R_i = 1.8 and 3.4 μm, the V^* values are both ~4.4Ω. Those for heterogeneous yielding at R_i = 3.4 and 8.2 μm are ~0.5Ω and ~0.7Ω, respectively. Similar results were also obtained for Grain 2, as shown in Fig. S2, again implying the trend observed in Fig. 7 is representative for this MEA. As expected, V^* is only dependent on the deformation mechanism, and not on R_i. V^* for homogeneous yielding is much larger than that for heterogeneous yielding. The V^* value for homogeneous yielding here (~4.4Ω) agrees well with that obtained in bcc HfNbTiZr HEA (~3–5Ω) in a prior study [33] where homogeneous yielding should prevail since a spherical tip with R_i = 0.27 μm was used and the τ_y data is narrowly distributed.

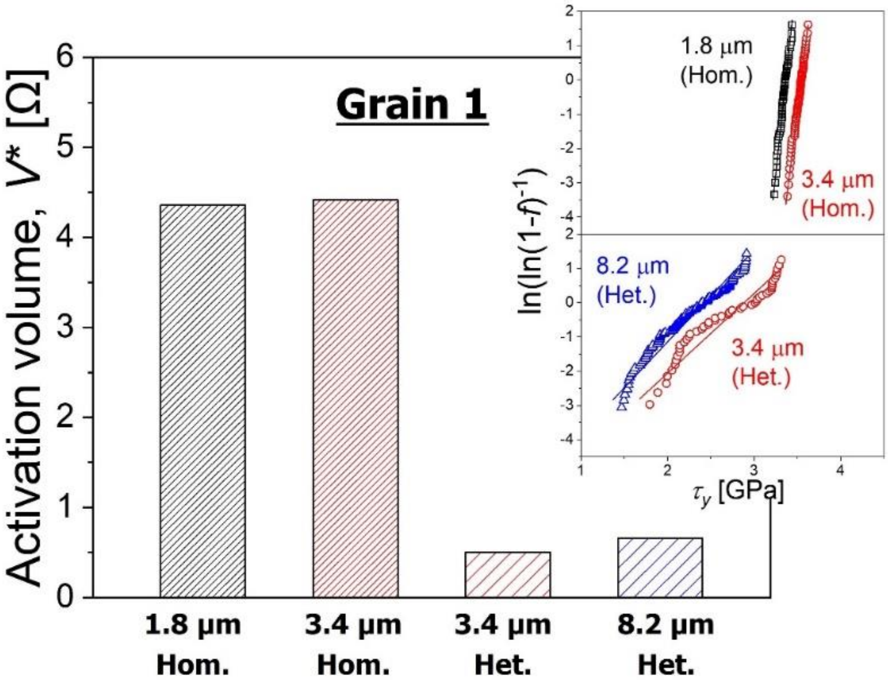

Fig. 7 Estimated activation volumes, V^*, normalized with the atomic volume Ω, obtained with different R_i. The insets show the linear fitting of ln[−ln(1−F)] vs. τ_y utilized for estimating V^*. (Het.: heterogeneous yielding, Hom.: homogeneous yielding)

5. Change in stochastic nature upon hydrogenation

To better understand the stochastic nature of the yielding, it is crucial to examine how it can be affected by either external environmental or internal metallurgical conditions of an alloy. For this purpose, hydrogenation can be one of the most effective ways, since it may conceivably change even the microstructure of the material. For this purpose, the statistical characters of the pop-in behavior before and after hydrogen charging are directly compared.

Nanoindentation tests with R_i = 1.8 and 3.4 μm at 0.25 mN/s were conducted on the hydrogen-charged samples under the same conditions as those utilized for the uncharged samples, and the results are shown in Figs. 8 and 9, respectively. They clearly show that after hydrogenation, the fraction of the data that corresponds to heterogeneous yielding becomes larger, as marked in Fig. 8c, at the cost of homogeneous yielding. For R_i = 1.8 μm (Fig. 8), while a similar spread in P_I is also observed in the charged sample (Fig. 8b) compared to that obtained on the uncharged one (Fig. 8a), the cumulative distribution in τ_y shows some difference. In the uncharged sample, the narrow distribution regime at relatively high stress for homogeneous yielding is predominant (~82.4% of the total data) and merely ~17.6% of the data corresponds to heterogeneous yielding (as illustrated by the blue lines in Fig. 8c). In the hydrogen-charged sample, however, the fraction of heterogeneous yielding regime becomes larger (~30.4% of the total data, as illustrated by the red lines in Fig. 8c). For R_i = 3.4 μm in Fig. 9, similar (and more obvious) trend is observed: while both heterogeneous and homogeneous yielding portions are observed in uncharged sample, only wide-spread heterogeneous yielding data at relatively lower stresses (below ~3.4 GPa, which is also approximately the lower threshold for the stress for homogeneous yielding in unchanged sample), could be seen (Fig. 9c). In all, irrespective R_i, the change in the statistical nature of the pop-in data demonstrates a shift in the governing yielding mechanism from homogeneous to heterogeneous yielding upon hydrogenation.

(a)

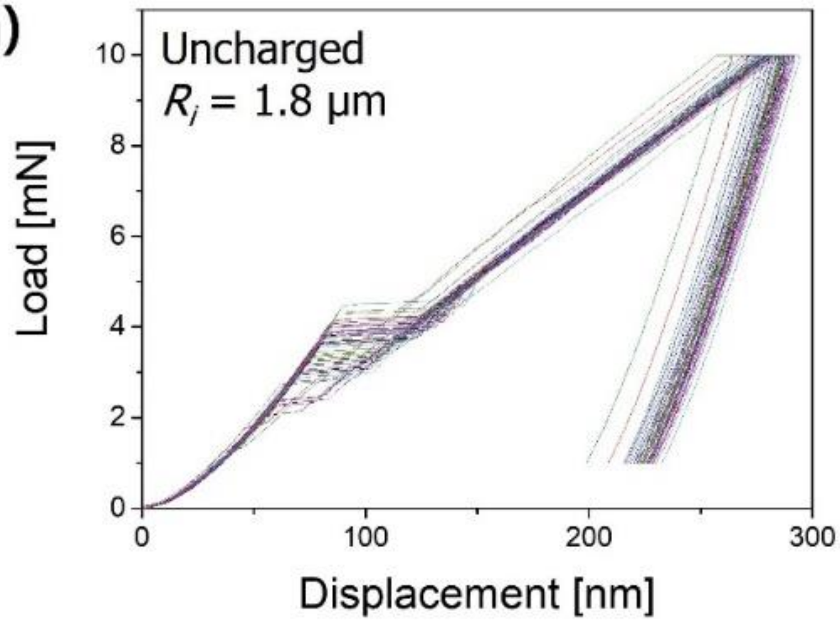

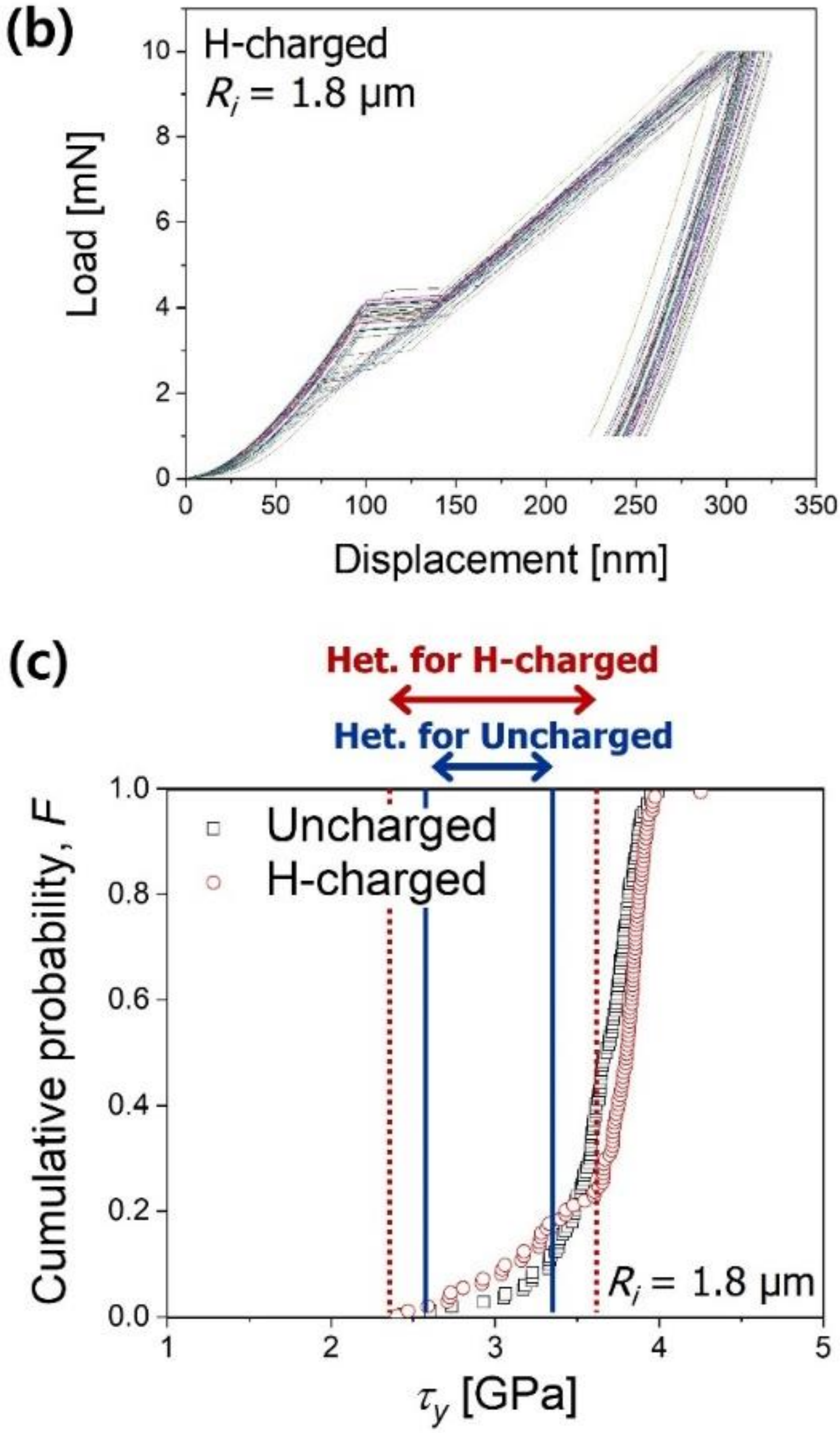

Fig. 8 *P-h* curves of (a) uncharged and (b) hydrogen-charged specimens, and (c) cumulative probability distribution of τ_y for R_i = 1.8 μm tested with a loading rate of 0.25 mN/s. (Het.: heterogeneous yielding, Hom.: homogeneous yielding)

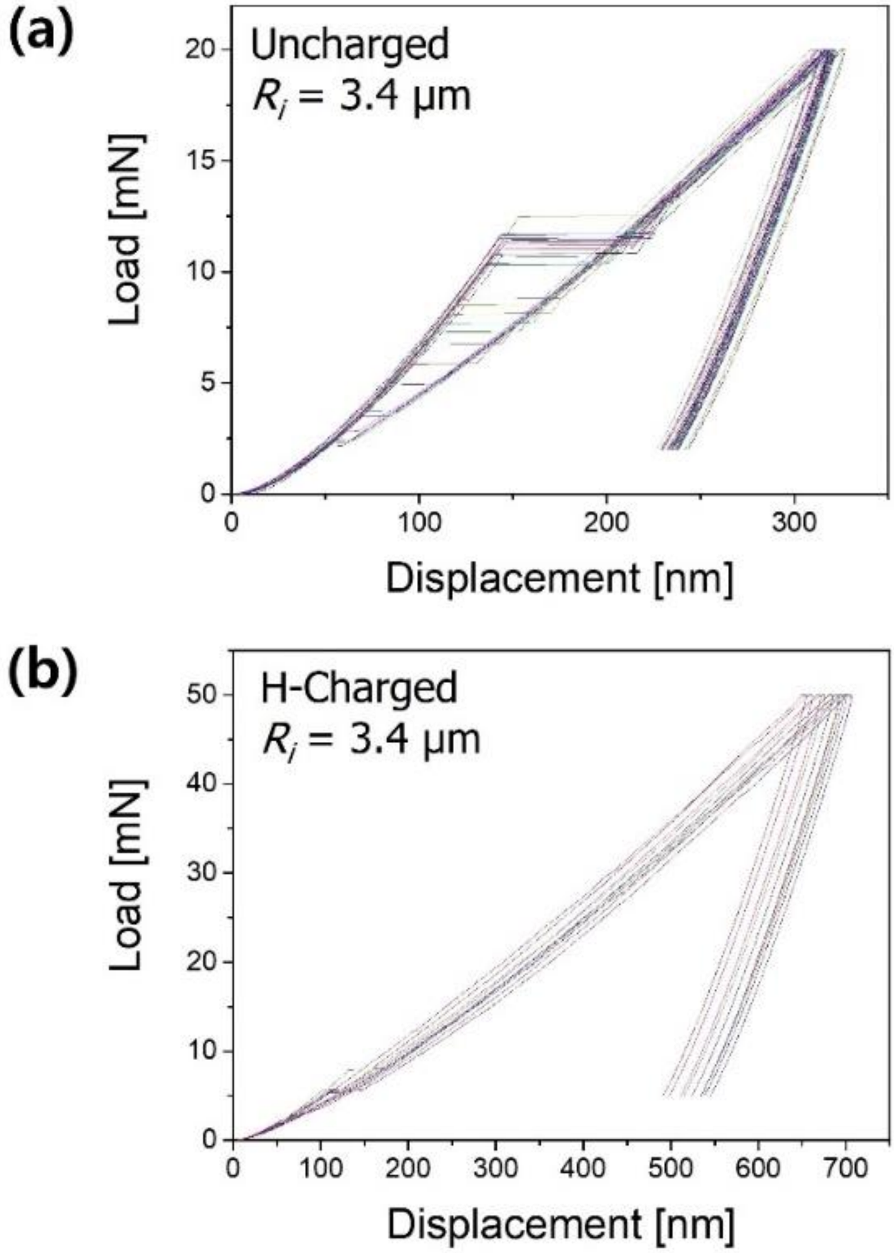
(a)
Uncharged
R_i = 3.4 μm
Load [mN]
Displacement [nm]
(b)
H-Charged
R_i = 3.4 μm
Load [mN]
Displacement [nm]

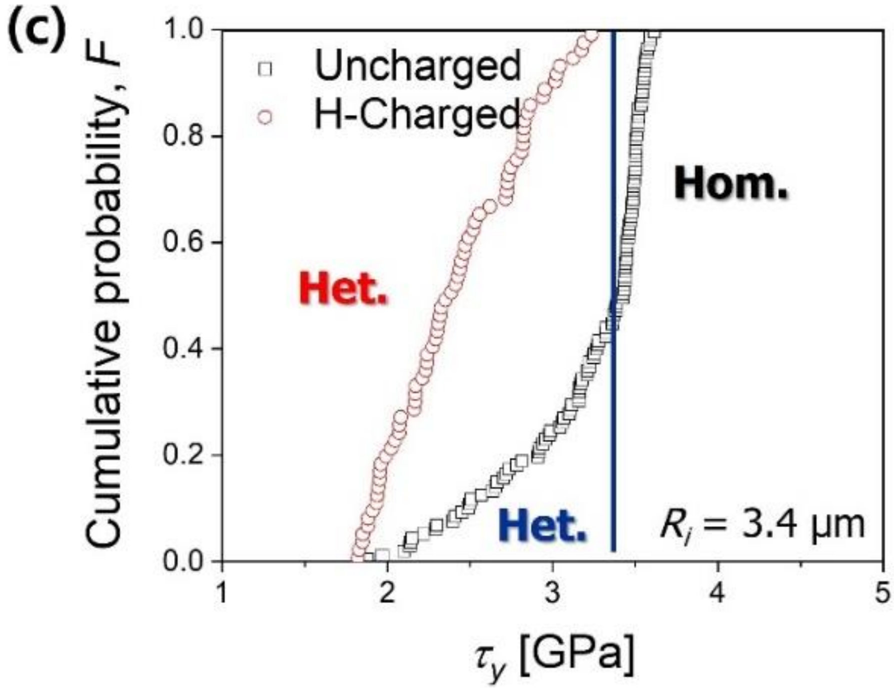

Fig. 9 *P-h* curves of (a) uncharged and (b) hydrogen-charged specimens, and (c) cumulative probability distribution of τ_y for R_i = 3.4 μm tested at a loading rate of 0.25 mN/s. (Het.: heterogeneous yielding, Hom.: homogeneous yielding)

The fact that hydrogen makes the MEA under investigation more favorable for heterogeneous yielding suggests the positive role of hydrogen in assisting (heterogeneous) dislocation nucleation and/or activation of their glide. This is in line with the thermodynamic framework of so-called "defactants" (originated from "DEFect ACTing AgeNTS" [36,37]), wherein hydrogen atoms preferentially segregate to the defect sites (such as dislocations, vacancies, grain boundaries, and voids) and, in turn, lower the activation energies for the formation of new defects (including dislocation loops and vacancies) in a manner similar to that by which solute molecules reduce surface energies in liquid [36,37]. For instance, it was reported that the dislocation density in an advanced high-strength steel increased significantly only upon hydrogen charging without any external stress [38]. Therefore, when a hydrogen-charged sample is deformed, more dislocations and vacancies are likely to be generated at the same stress level as compared to the case in an uncharged sample. In such a case, the heterogeneous yielding aided by these defects would thus become easier.

To gain further experimental support for the above scenario, TEM was used to characterize the dislocation behavior underneath the indent performed with R_i = 3.4 μm, i.e., the case where both homogeneous and heterogeneous yielding can occur, with the probability of each depending on the size of the highly stressed region relative to the spacing of the defects. It should be noted here that there are two difficulties associated with a "proper" TEM observation of the behavior right after pop-in. First, the dislocation multiplication during the continued loading after the pop-in event can alter the deformation features underneath the indenter. Thus, the cross-sectional TEM images must be taken from the indents where unloading is made right after the first pop-in. Second, during cross-sectioning of indents by FIB milling for preparing the TEM specimens, the Ga ions that are typically used for the milling can damage the surface, which would affect the subsequent TEM observations of dislocations.

To overcome the above-mentioned difficulties, nanoindentation tests were first conducted at P_{max} = 5 and 11 mN, respectively, for over 100 trials per condition on uncharged and hydrogen-charged samples. These two P_{max} values were selected because their corresponding τ_y values are 2.7 and 3.6 GPa, respectively, corresponding to heterogeneous and homogeneous yielding respectively in the uncharged sample. However, they both correspond to the heterogeneous yielding condition in the hydrogen-charged sample, as evidenced in Fig. 9c. Then, the nanoindentation tests where the first pop-in occurs right at or near P_{max} were selected for the TEM analysis (see the *P*-*h* curves in Figs. 11 and 12). Successive FIB sampling was conducted at two stages, i.e., first, rough milling with Ga ion and then finalizing with Ar ion. The milling with Ar ion was adopted to reduce the ion damage on the sample surface [27].

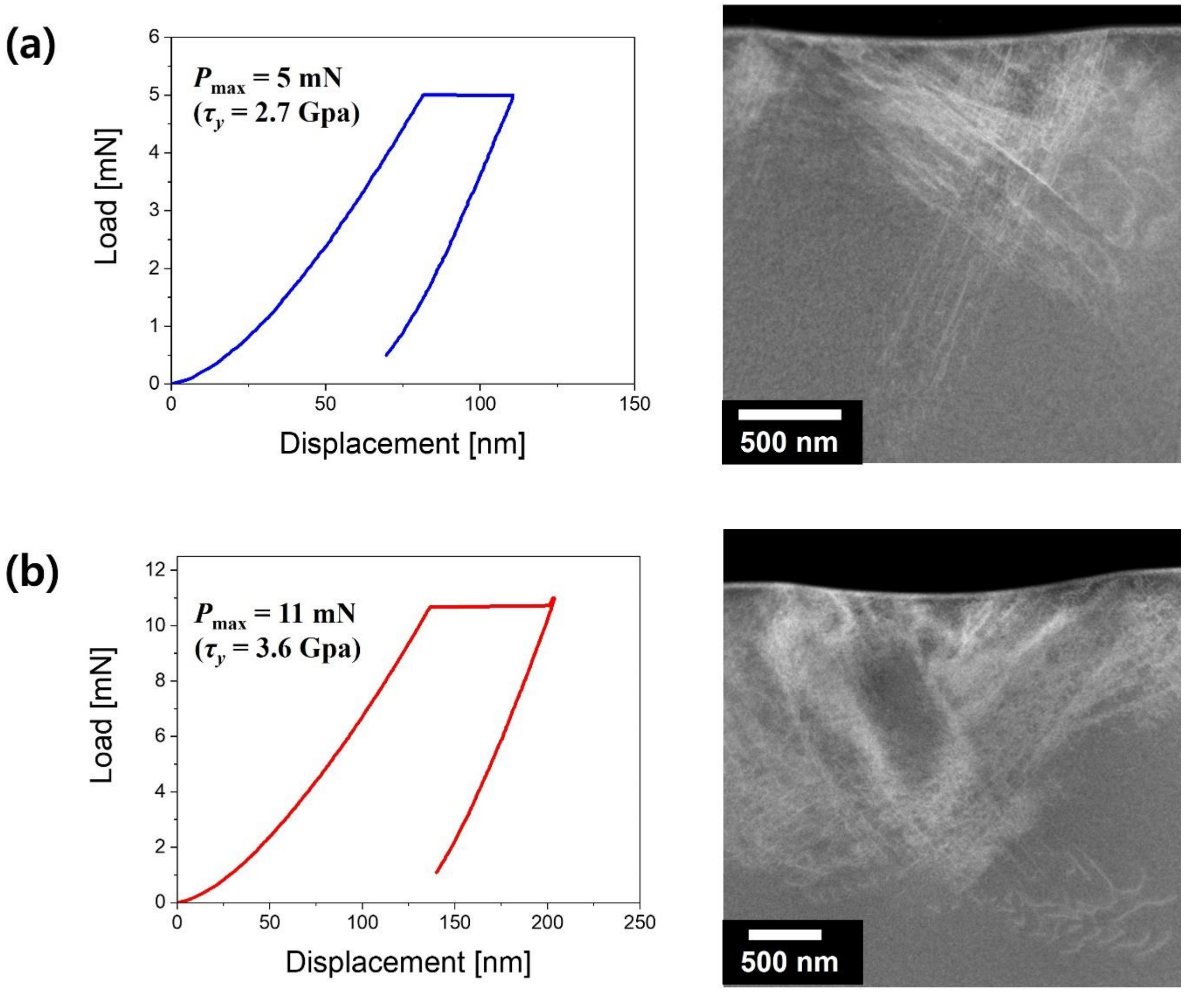

Fig. 10 *P-h* curves and corresponding STEM images of the region underneath the indenter for uncharged sample at (a) $P_{\max}$ = 5 and (b) 11 mN. Zone axis = [110].

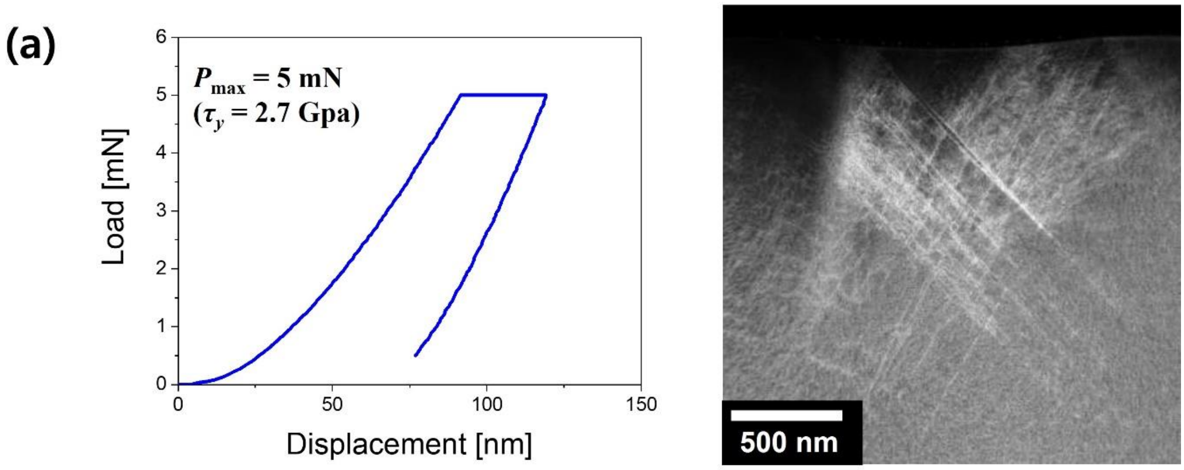

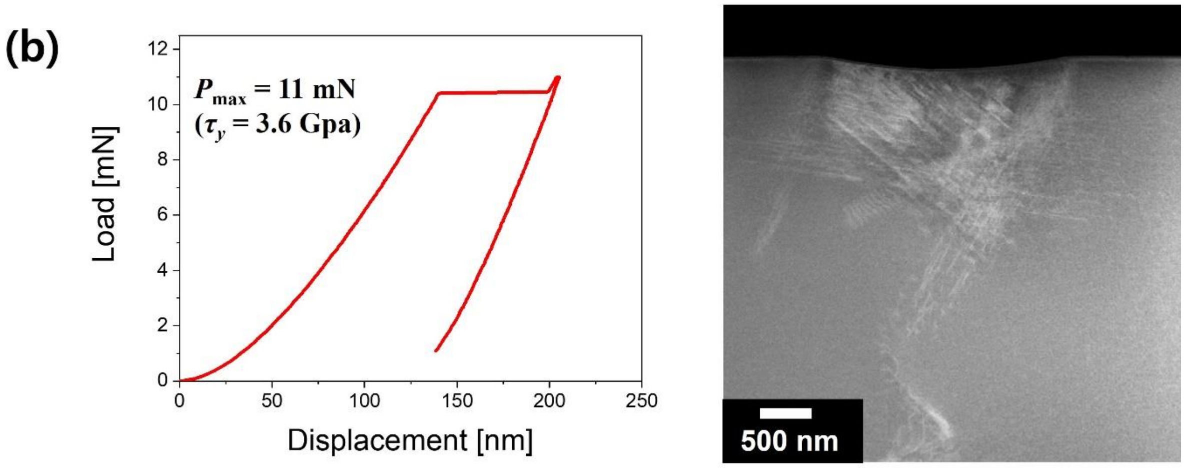

Fig. 11 *P-h* curves and corresponding STEM images of the region underneath the indenter for hydrogen-charged sample at (a) P_{max} = 5 and (b) 11 mN. Zone axis = [110].

Fig. 10 shows the cross-sectional scanning TEM (STEM) images for the specimens before hydrogen charging. In the indentation performed with P_{max} = 5 mN, which corresponds to heterogeneous yielding (Fig. 10a), clear slip lines beneath the indenter are seen. They indicate a micron-scale plasticity event due to planar slip of pre-existing dislocations. Similar behavior can also be noted in Figs. 11a and 11b, where hydrogen-charged samples also show dislocation planar slip traces clearly. In sharp contrast, in the indent made with P_{max} = 11 mN, which corresponds to homogenous yielding (Fig. 10b), more homogenized and disperse dislocations were found, without any clear traces of planar slip. Such a larger dislocation volume formed suggests homogeneous yielding from an initially defect-free region, followed by more homogeneously distributed dislocation field development.

To further elucidate the underlying mechanisms for the observed evolution in pop-in behavior, additional statistical analysis is conducted. With R_i = 3.4 μm, where an obvious change in τ_y distribution was noticed (Fig. 9c), the probability distribution of the data before and after H charging were obtained using the kernel density estimates (KDEs) [22,39], as shown in Fig. 12. The shapes of the uncharged and hydrogen charged plots show three and two peaks, respectively. Therefore, the data were deconvoluted assuming that it is Gaussian in its nature, as also shown in Fig. 12. The peak number 3 in the uncharged sample (green dashed curve in Fig. 12a) corresponds to the homogeneous yielding (as shown in Figs. 6b and 7). The heterogeneous yielding requiring relatively lower stress can be deconvoluted into two peaks (peaks 1 and 2) in both the samples. Following the methodology described in reference [39], by computing the F values for each of the deconvoluted Gaussian distribution and then plotting $\ln[-\ln(1-F)]$ versus τ_y for that particular distribution, the activation volume V^* associated with each of the deconvoluted peak is obtained using Eq. (2). Values of the V^* normalized by the atomic volume, Ω, are displayed alongside the corresponding peak in Fig. 12. Two distinct levels of V^* occurring at ~0.6–0.7Ω and ~1.0–1.2Ω could be noted.

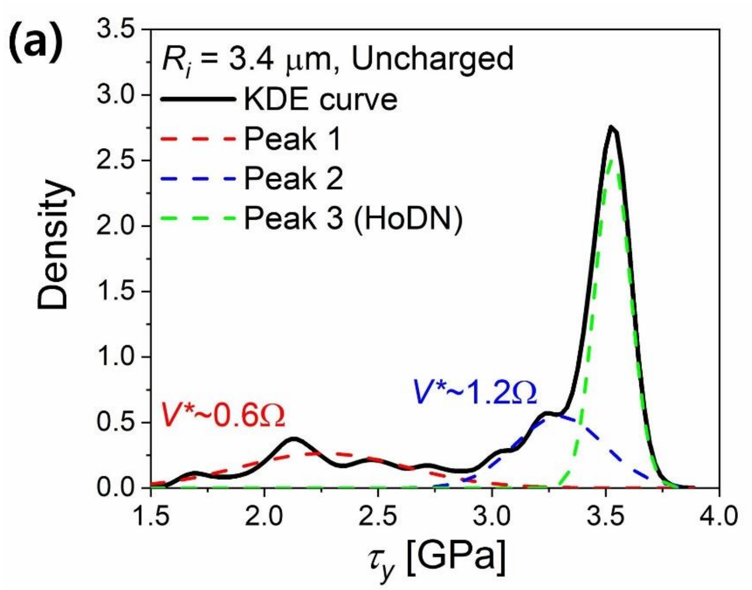

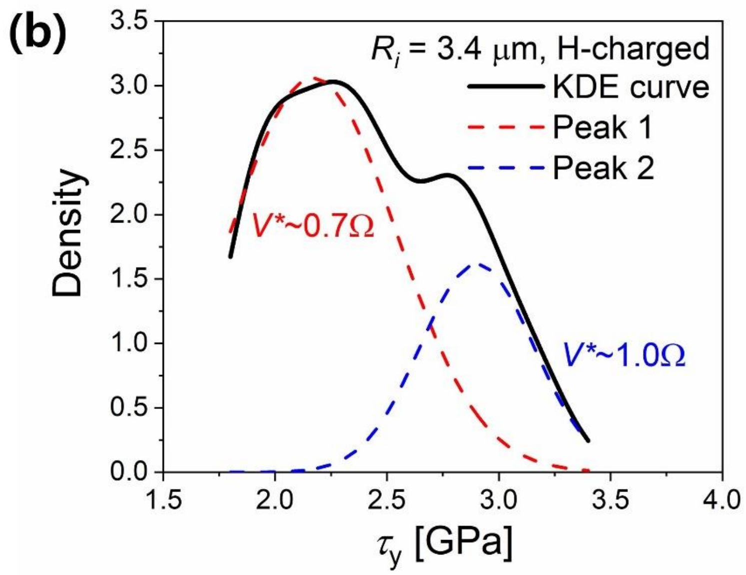

Fig. 12 The KDE curves and the deconvoluted Gaussian distributions for the results obtained with R_i = 3.4 μm on the (a) uncharged and (b) hydrogen charged samples, with the $V*$ of each peak given in terms of Ω for the heterogeneous yielding peaks.

Most of the published work on the pop-in behavior in crystalline alloys [10,12,17,33,34] indicates that the presence of pre-existing defects such as vacancies, vacancy clusters, immobile dislocations, and impurities could aid in heterogeneous dislocation nucleation that leads to the pop-in. It is possible that such a mechanism is responsible for the low strength peak (peak 1) observed in Fig. 12. To understand the type of defect that is responsible for the pop-in, a mathematical estimate of the defect density can be made. First, we assume that a certain type of defect is responsible for the peak observed at lower strength (peak 1), and that pop-in will only occur if and only if at least one such defect exists within the highly stressed volume underneath the spherical indenter, V_s, (= πa_c^3 [12,39], where $a_c = \sqrt[3]{3P_I R_i/(4E_r)}$ is the contact radius). This then allows the use of the exponential (or Poisson) distribution statistics to estimate the probability for the existence of such a defect, P_{low}, within V_s [9,38] as

$$P_{low} = 1 - \exp(-\rho_{low} V_s) \quad (4)$$

where ρ_{low} is the number density of the specific defect per unit volume. Based on the data in this study, as listed in Table 2, the average spacing between the defects, $l_{low} = 1/\sqrt[3]{\rho_{low}}$, is estimated as ~0.94 and ~0.54 nm, respectively, for $R_i = 3.4$ µm tests before and after H charging. Similarly, l_{low} is estimated as ~1.25 µm for nanoindentation tests with R_i = 8.2 µm on the uncharged sample, as also listed in Table 2. Taking dislocation density, ρ_{disl}, in each sample of the order of ~10^{12} m^{-2} that is typical in annealed metals [39], the mean spacing between the dislocations, $l_{disl} = 1/\sqrt{\rho_{disl}}$ would be ~1 µm. The similarity in l_{low} and l_{disl} values supports the possibility of a heterogeneous yielding mechanism originated from a pre-existing dislocation being responsible for the peak 1 in Fig. 12. For peak 2 in Fig. 12, it is important to recognize here that the above estimation and its assumptions will hold true only for the defect that would get activated at the lowest-stress (for peak 1) as it would be the first one to get triggered even if there are higher-stress defects (for peak 2) present in V_s. Although it lacks a more direct experimental proof, the fact that the V^* values are close to 1Ω may suggest a monovacancy-mediated heterogeneous yielding mechanism for peak 2 [34].

Table 2. Summary of the peak 1 fraction, V_s, ρ_{low}, and l_{low} values estimated for uncharged and H-charged samples.

Sample	R_i [µm]	Peak 1 fraction	V_s [µm^3]	ρ_{low} [µm^{-3}]	l_{low} [µm]
Uncharged	3.4	0.24	0.23	1.20	0.94
	8.2	0.70	2.37	0.51	1.25
H-charged	3.4	0.74	0.20	6.51	0.54

All the above results clearly point towards the fact that the elastic-to-elastoplastic transition behavior of materials at small length scales should be statistically analyzed; otherwise, incorrect conclusions are likely to be drawn. In such an analysis, the distributions of defects play a vital role and the change in the size of the stressed volume can provide some solid evidence, which also holds valid in this first investigation on single crystal bcc MEA. In this line, before closing, it is constructive to briefly discuss and compare this stochastic nature of incipient plasticity behavior between bcc and fcc H/MEAs. While for both bcc and fcc H/MEAs, there can be multiple mechanisms responsible for small-scale incipient plasticity (corresponding to multimodal distributions in τ_y values) depending on R_i as well as microstructural states (e.g. defect densities) [39]. A distinct feature of the bcc NbTiZr MEA investigated here, however, is the very narrow range of P_I and τ_y values for the homogeneous dislocation nucleation. This is different from the case in fcc CoCrFeNi and CoCrFeMnNi HEAs [36] where homogeneous yielding manifests with a rather broad τ_y distribution. This corresponds well with the prior experimental results on bcc Mo and fcc Ni single crystals [26]. In this sense, it is not so different between HEAs/MEAs and conventional metals and alloys, and the most likely reason is that partial dislocations, instead of full dislocations (as in bcc metals and alloys), are responsible for the dislocation nucleation behavior in fcc metals and alloys, which can be manifest as successive pop-ins in them [28,39]. Such distinct characteristic with bcc actually makes it more proper for comparative study on the homogeneous versus heterogeneous yielding behavior. A potential difference between HEAs/MEAs and conventional metals and alloys may be that the lattice distortion and hence, more vacancies in the former may make them more prone to vacancy-mediated dislocation nucleation mechanism [26,33,34]. Such a mechanism, nevertheless, should only affect the relative portion for the vacancy-related peak in the bi- or multi-modal distributions (like those displayed in Fig. 12). Thus, it will not alter the main conclusions we reached in the present study. It is also noteworthy that short-range ordering, that has been frequently observed in HEAs/MEAs [39–41], could also influence the pop-in behavior and its statistics. However, the effect of SRO is not specifically explored in the present work, since we did not observe any strong or direct evidence to prove or disprove it. Moreover, the critical role of hydrogen in altering the incipient plasticity mechanisms is also highlighted here based on the current results. The fact that heterogeneous yielding, being either the activation of pre-existing dislocations or the dislocation nucleation aided by pre-existing defects, is enhanced by hydrogen charging demonstrated the effect of hydrogen on promoting the defect formation, as previously theoretically sketched in “defactant” thermodynamic framework.

6. Conclusions

In this study, nanoindentation tests using spherical indenters with different radii (1.8, 3.4, and 8.2 μm) were conducted within a single grain NbTiZr medium-entropy alloy to analyze the microscopic yield behavior. Changes in the indenter radius led to variations in the shape of the cumulative probability distributions of the first pop-in load and the corresponding maximum shear stress τ_y. Such a change in τ_y distribution is dominated by the micromechanisms responsible for the incipient plasticity, which, in turn, depends on the volume of the material underneath the indenter that is being probed. Based on a detailed statistical analysis and data deconvolution, homogeneous and heterogeneous yielding mechanisms, where the latter includes both the nucleation from and the glide of pre-existing dislocations, respectively were found to be responsible for the narrow high-stress regime and the broad low-stress regime obtained by deconvoluting the peaks in τ_y distribution.

Upon subsequent hydrogen charging, while τ_y shows an overall reduction, the portion of heterogeneous yielding becomes more significant and dominant, indicating hydrogen-enhanced defect formation, which is in line with the “defactants” thermodynamic framework. The suggested scenario for how the mechanisms are affected by the stressed volume and hydrogen-induced structural change was confirmed by direct observation of the deformation behavior underneath the indenter with transmission electron microscopy.

Acknowledgements

The work at Hanyang University was supported by the National Research Foundation of Korea (NRF) grants funded by the Korea government (MSIT) (No. 2022R1A5A1030054 and RS-2023-00273384). The work at KIST was supported by Creative Materials Discovery Program through the NRF grants funded by the MSIT (No. NRF-2019M3D1A1079225). The work at KAIST was supported by the NRF grants funded by the MSIT (No. 2021R1A2C2014025 and 2022R1A5A1030054). The work at POSTECH was supported by the NRF grant funded by the MSIP (No. 2021R1A2C3006662 and 2022R1A5A1030054). UR and YZ acknowledge the support from the Structural Metal Alloys Program (Grant reference No.: A18B1b0061) of the Agency for Science, Technology and Research (A*STAR) of Singapore.

References

1. W.C. Oliver, G.M. Pharr, An improved technique for determining hardness and elastic modulus using load and displacement sensing indentation experiments, J. Mater. Res. 7 (1992) 1564–1583. https://doi.org/10.1557/JMR.1992.1564.
2. Y. Gao, H. Bei, Strength statistics of single crystals and metallic glasses under small stressed volumes, Prog. Mater. Sci. 82 (2016) 118–150. https://doi.org/10.1016/j.pmatsci.2016.05.002.
3. T. Rouxel, J. Jang, U. Ramamurty, Indentation of glasses, Prog. Mater. Sci. 121 (2021) 100834. https://doi.org/10.1016/j.pmatsci.2021.100834.
4. T.F. Page, W.C. Oliver, C.J. McHargue, The deformation behavior of ceramic crystals subjected to very low load (nano)indentations, J. Mater. Res. 7 (1992) 450–473. https://doi.org/10.1557/JMR.1992.0450.
5. M.K. Mishra, G.R. Desiraju, U. Ramamurty, A.D. Bond, Studying Microstructure in Molecular Crystals With Nanoindentation: Intergrowth Polymorphism in Felodipine, Angew. Chemie. 126 (2014) 13318–13321. https://doi.org/10.1002/ange.201406898
6. M.K. Mishra, U. Ramamurty, G.R. Desiraju, Mechanical property design of molecular solids, Curr. Opin. Solid State Mater. Sci. 20 (2016) 361–370. https://doi.org/10.1016/j.cossms.2016.05.011.
7. P. Sudharshan Phani, K.E. Johanns, E.P. George, G.M. Pharr, A stochastic model for the size dependence of spherical indentation pop-in, J. Mater. Res. 28 (2013) 2728–2739. https://doi.org/10.1557/jmr.2013.254.
8. P. Sudharshan Phani, K.E. Johanns, E.P. George, G.M. Pharr, A simple stochastic model for yielding in specimens with limited number of dislocations, Acta Mater. 61 (2013) 2489–2499. https://doi.org/10.1016/j.actamat.2013.01.023.
9. J.R. Morris, H. Bei, G.M. Pharr, E.P. George, Size Effects and Stochastic Behavior of Nanoindentation Pop In, Phys. Rev. Lett. 106 (2011) 165502. https://doi.org/10.1103/PhysRevLett.106.165502.
10. T.L. Li, H. Bei, J.R. Morris, E.P. George, Y.F. Gao, Scale effects in convoluted thermal/spatial statistics of plasticity initiation in small stressed volumes during

nanoindentation, Mater. Sci. Technol. (United Kingdom). 28 (2012) 1055–1059. https://doi.org/10.1179/1743284712Y.0000000007.

11. C.A. Schuh, J.K. Mason, A.C. Lund, Quantitative insight into dislocation nucleation from high-temperature nanoindentation experiments, Nat. Mater. 4 (2005) 617–621. https://doi.org/10.1038/nmat1429.
12. J.K. Mason, A.C. Lund, C.A. Schuh, Determining the activation energy and volume for the onset of plasticity during nanoindentation, Phys. Rev. B - Condens. Matter Mater. Phys. 73 (2006) 1–14. https://doi.org/10.1103/PhysRevB.73.054102.
13. S. Shim, H. Bei, E.P. George, G.M. Pharr, A different type of indentation size effect, Scr. Mater. 59 (2008) 1095–1098. https://doi.org/10.1016/j.scriptamat.2008.07.026.
14. G.E. Dieter, Mechanical Metallurgy, McGraw-Hill, New York, 1961. https://doi.org/10.5962/bhl.title.35895.
15. Y. Xia, Y. Gao, G.M. Pharr, H. Bei, Single versus successive pop-in modes in nanoindentation tests of single crystals, J. Mater. Res. 31 (2016) 2065–2075. https://doi.org/10.1557/jmr.2016.193.
16. H. Bei, Y.Z. Xia, R.I. Barabash, Y.F. Gao, A tale of two mechanisms: Strain-softening versus strain-hardening in single crystals under small stressed volumes, Scr. Mater. 110 (2016) 48–52. https://doi.org/10.1016/j.scriptamat.2015.07.043.
17. X. Xiao, L. Yu, A unified statistical model for indentation pop-in: Effects of indenter radius and microstructure density on the transition from homogeneous nucleation to heterogeneous nucleation to bulk plasticity, Int. J. Plast. 141 (2021) 102980. https://doi.org/10.1016/j.ijplas.2021.102980.
18. H. Bei, Y.F. Gao, S. Shim, E.P. George, G.M. Pharr, Strength differences arising from homogeneous versus heterogeneous dislocation nucleation, Phys. Rev. B - Condens. Matter Mater. Phys. 77 (2008) 2–5. https://doi.org/10.1103/PhysRevB.77.060103.
19. B.D. Beake, S. Goel, Incipient plasticity in tungsten during nanoindentation: Dependence on surface roughness, probe radius and crystal orientation, Int. J. Refract. Met. Hard Mater. 75 (2018) 63–69.

https://doi.org/10.1016/j.ijrmhm.2018.03.020.

20. H. Bei, Z.P.P. Lu, S. Shim, G. Chen, E.P.P. George, Specimen Size Effects on Zr-Based Bulk Metallic Glasses Investigated by Uniaxial Compression and Spherical Nanoindentation, Metall. Mater. Trans. A. 41 (2010) 1735–1742. https://doi.org/10.1007/s11661-009-9994-y.
21. I.-C. Choi, Y. Zhao, Y.-J. Kim, B.-G. Yoo, J.-Y. Suh, U. Ramamurty, J. Jang, Indentation size effect and shear transformation zone size in a bulk metallic glass in two different structural states, Acta Mater. 60 (2012) 6862–6868. https://doi.org/10.1016/j.actamat.2012.08.061.
22. S. Nag, R.L. Narayan, J. Jang, C. Mukhopadhyay, U. Ramamurty, Statistical nature of the incipient plasticity in amorphous alloys, Scr. Mater. 187 (2020) 360–365. https://doi.org/10.1016/j.scriptamat.2020.06.045.
23. L. Huang, D. Chen, D. Xie, S. Li, Y. Zhang, T. Zhu, D. Raabe, E. Ma, J. Li, Z. Shan, Quantitative tests revealing hydrogen-enhanced dislocation motion in α-iron, Nat. Mater. 22 (2023) 710–716. https://doi.org/10.1038/s41563-023-01537-w.
24. H. Luo, Z. Li, D. Raabe, Hydrogen enhances strength and ductility of an equiatomic high-entropy alloy, Sci. Rep. 7 (2017) 1–7. https://doi.org/10.1038/s41598-017-10774-4.
25. M. Nagumo, Hydrogen related failure of steels – a new aspect, Mater. Sci. Technol. 20 (2004) 940–950. https://doi.org/10.1179/026708304225019687.
26. G. Yang, Y. Zhao, D.-H. Lee, J.-M. Park, M.-Y. Seok, J.-Y. Suh, U. Ramamurty, J. Jang, Influence of hydrogen on incipient plasticity in CoCrFeMnNi high-entropy alloy, Scr. Mater. 161 (2019) 23–27. https://doi.org/10.1016/j.scriptamat.2018.10.010.
27. Z. Huang, Combining Ar ion milling with FIB lift-out techniques to prepare high quality site-specific TEM samples, J. Microsc. 215 (2004) 219–223. https://doi.org/10.1111/j.0022-2720.2004.01376.x.
28. L. Wang, H. Bei, T.L. Li, Y.F. Gao, E.P. George, T.G. Nieh, Determining the activation energies and slip systems for dislocation nucleation in body-centered cubic Mo and face-centered cubic Ni single crystals, Scr. Mater. 65 (2011) 179–182.

https://doi.org/10.1016/j.scriptamat.2011.03.036.

29. J.-i. Jang, H. Bei, P.F. Becher, G.M. Pharr, Experimental analysis of the elastic-plastic transition during nanoindentation of single crystal alpha-silicon nitride, J. Am. Ceram. Soc. 95 (2012) 2113–2115. https://doi.org/10.1111/j.1551-2916.2012.05251.x
30. K.L. Johnson, Contact Mechanics, Cambridge University Press, Cambridge, 1985. https://doi.org/10.1017/CBO9781139171731.
31. C.A. Schuh, A.C. Lund, Application of nucleation theory to the rate dependence of incipient plasticity during nanoindentation, J. Mater. Res. 19 (2004) 2152–2158. https://doi.org/10.1557/JMR.2004.0276.
32. Y. Zhao, I.-C. Choi, M.-Y. Seok, M.-H. Kim, D.-H. Kim, U. Ramamurty, J.-Y. Suh, J. Jang, Effect of hydrogen on the yielding behavior and shear transformation zone volume in metallic glass ribbons, Acta Mater. 78 (2014) 213–221. https://doi.org/10.1016/j.actamat.2014.06.046.
33. Y.X. Ye, Z.P. Lu, T.G. Nieh, Dislocation nucleation during nanoindentation in a body-centered cubic TiZrHfNb high-entropy alloy, Scr. Mater. 130 (2017) 64–68. https://doi.org/10.1016/j.scriptamat.2016.11.019.
34. C. Zhu, Z.P. Lu, T.G. Nieh, Incipient plasticity and dislocation nucleation of FeCoCrNiMn high-entropy alloy, Acta Mater. 61 (2013) 2993–3001. https://doi.org/10.1016/j.actamat.2013.01.059.
35. M. Akmal, H.W. Seong, H.J. Ryu, Mo and Ta addition in NbTiZr medium entropy alloy to overcome tensile yield strength-ductility trade-off, J. Mater. Sci. Technol. 109 (2022) 176–185. https://doi.org/10.1016/j.jmst.2021.08.073.
36. R. Kirchheim, Revisiting hydrogen embrittlement models and hydrogen-induced homogeneous nucleation of dislocations, Scr. Mater. 62 (2010) 67–70. https://doi.org/10.1016/j.scriptamat.2009.09.037.
37. A. Barnoush, H. Vehoff, Recent developments in the study of hydrogen embrittlement: Hydrogen effect on dislocation nucleation, Acta Mater. 58 (2010) 5274–5285. https://doi.org/10.1016/j.actamat.2010.05.057.
38. P. Gong, A. Turk, J. Nutter, F. Yu, B. Wynne, P. Rivera-Diaz-del-Castillo, W.M. Rainforth, Hydrogen embrittlement mechanisms in advanced high strength steel, Acta Mater. 223

(2022) 117488.
https://doi.org/10.1016/j.actamat.2021.117488

39. Y. Zhao, J.-M. Park, J. Jang, U. Ramamurty, Bimodality of incipient plastic strength in face-centered cubic high-entropy alloys, Acta Mater. 202 (2021) 124–134. https://doi.org/10.1016/j.actamat.2020.10.066.
40. Q. Zhang, X. Jin, X.H. Shi, J.W. Qiao, P.K. Liaw, Short range ordering and strengthening in CoCrNi medium-entropy alloy, Mater. Sci. Eng. A 854 (2022) 143890. https://doi.org/10.1016/j.msea.2022.143890
41. Q. Zhang, P.K. Liaw, H.J. Yang, J.W. Qiao, Short range ordering and the evolution of dislocation-nucleation modes in an $Fe_{40}Mn_{20}Cr_{20}Ni_{20}$ high-entropy alloy, Mater. Sci. Eng. A 873 (2024) 145038. https://doi.org/10.1016/j.msea.2023.145038